https://doi.org/10.5194/egusphere-2026-2447
Preprint. Discussion started: 3 July 2026

Mass-constrained source apportionment of nitrate-containing particles in eastern China using a SPAMS-NMF framework

Wenfei Zhu[1,2], Qinghong Wang[1], Qingsong Wang[3], Jialin Shi[1], Yu Sun[1], Juntao Huo[4], Yi Sun[4], Jia Chen[4], Yue Zhao[4], Mei Li[5], Jun Chen[1], Shengrong Lou[1*], Hui Chen[3]*

[1]School of Energy and Power Engineering, University of Shanghai for Science and Technology, Shanghai 200093, China P. R.
[2]Institute of Climate and Energy Research, ICE-3: Troposphere, Forschungszentrum, Jülich, 52425 Jülich, Germany
[3]School of Environmental and Chemical Engineering, Shanghai University, Shanghai, 200444, China P. R.
[4]Shanghai Environmental Monitoring Center, Shanghai, 200235, China P. R.
[5]Institute of Mass Spectrometry and Atmospheric Environment, Guangdong Provincial Engineering Research Center for On-line Source Apportionment System of Air Pollution, Jinan University, Guangzhou 510632, China P. R.

Correspondence to: Shengrong Lou (lousr@usst.edu.cn); Hui Chen (huichen@shu.edu.cn)

Abstract. Winter haze in eastern China is increasingly dominated by particulate nitrate, but its compositions and source contributions remain poorly constrained. We conducted intensive winter observations at a regional site in suburban Shanghai and developed a semi-quantitative single-particle framework combining SPAMS with factor analysis to attribute nitrate to specific particle types and sources in near real time. Nitrate occurred mainly in the accumulation mode (~0.5–0.7 μm), implying high regional persistence. Four nitrate-containing particle classes (NO_3Lv1–Lv4) were identified. A highly aged class (NO_3Lv4) accounted for the largest fraction of both particle number and nitrate mass loadings. This class showed extensive internal mixing with elemental carbon, ammonium, potassium-rich combustion markers, and chloride-depleted sea salt, indicating coupling between secondary inorganic nitrate, combustion emissions, and processed marine aerosol. Episode analysis and factorization further revealed that severe nitrate build-up reflects the co-occurrence of stagnant boundary layers, humid nocturnal heterogeneous formation of both ammonium and non-ammonium nitrate, long-range transport from northern industrial and urban corridors, and marine influence. These results indicate that winter nitrate haze in the Yangtze River Delta is governed by joint NO_x–NH_3 chemistry, primary combustion, and regional transport, requiring coordinated multipollutant control.

Keywords. Nitrate-containing particles, Non-negative matrix factorization, Source variations, Size distribution, SPAMS

1 Introduction

Particulate matter pollution, specifically $PM_{2.5}$, remains a significant environmental and public health issue in China, particularly in large urban areas(Yang and Bao, 2025; Zhang et al., 2022; Geng et al., 2021; Zhang et al., 2012). While there have been notable reductions in sulfur dioxide (SO_2) emissions over the last decade, resulting in decreased sulfate levels(Zheng et al., 2018), nitrate has emerged as a predominant component of $PM_{2.5}$, often constituting more than 20-30% of particle mass

https://doi.org/10.5194/egusphere-2026-2447
Preprint. Discussion started: 3 July 2026

during severe haze episodes(Xu et al., 2019; Xie et al., 2022; Song et al., 2019; Fu and Wang, 2020). The rapid rise in nitrate levels not only worsens haze formation but also impacts atmospheric oxidative processes, nitrogen cycles, and radiative forcing by increasing light scattering and hygroscopic properties(Xie et al., 2020; Ren et al., 2021b). Therefore, comprehending the formation mechanisms and sources of nitrate-containing particles is crucial for devising effective pollution control measures. Extensive field observations and modeling have revealed the intricate dynamics governing particulate nitrate formation(Li et al., 2021b; Xie et al., 2022). Particulate nitrate exhibits pronounced nonlinear responses to precursor controls, as reductions in nitrogen oxides (NOx) do not necessarily result in proportional decreases in nitrate levels due to the abundance of ammonia and shifts in atmospheric oxidizing capacity(Guo et al., 2018). For instance, significant NO_x emission cuts during the COVID-19 lockdown led to higher ozone and OH levels (from reduced NO titration), which, coupled with abundant NH_3, offset nitrate reductions and even increased nitrate formation in some regions(Ren et al., 2021a). Such phenomena underscore why nitrate has become one of the most challenging secondary inorganic aerosols to mitigate in China. Heterogeneous reactions (e.g. N_2O_5 hydrolysis at night) and regional transport further complicate nitrate formation pathways, often making simple precursor controls less effective(Xie et al., 2022).

While bulk chemical analyses have provided insights into overall nitrate levels, they fail to resolve particle-level heterogeneity. Advances in single-particle techniques, such as single-particle mass spectrometry (SPAMS), have demonstrated that particle composition is rarely present alone. Instead, particle composition is typically internally mixed with carbonaceous material, dust, sea salt, or metal-rich particles – pointing to diverse sources and complex atmospheric processing(Lian et al., 2025; Xiong et al., 2023). SPAMS has been particularly instrumental in investigating the mixing state, temporal dynamics, and potential sources of inorganic and organic containing particles(Sun et al., 2023; Cheng et al., 2018; Zhou et al., 2023). However, a key limitation of SPAMS is its semi-quantitative nature, as the technique inherently records particle counts and relative ion intensities rather than mass concentrations(Zhang et al., 2024; Zhou et al., 2020; Li et al., 2023). Consequently, direct quantitative source apportionment using SPAMS data alone remains challenging and bridging the gap between particle number information and chemically resolved mass concentrations limits their direct use in quantitative source apportionment.

In this study, we developed a mass-constrained based semi-quantitative optimization framework that integrates data with single-particle aerosol mass spectrometry (SPAMS) observations in Shanghai during autumn and winter. This approach enhances the conversion of particle number data into mass concentrations, facilitating more accurate source apportionment. Employing a non-negative matrix factorization (NMF) model, we quantitatively assessed the contributions of different sources to nitrate aerosols. Our findings offer new insights into the chemical composition, temporal dynamics, and source contributions of nitrate-containing particles under polluted conditions in the Yangtze River Delta.

https://doi.org/10.5194/egusphere-2026-2447
Preprint. Discussion started: 3 July 2026

2 Methods and Materials

2.1 Sampling site

The field campaign was conducted at the Dianshan Lake Atmospheric Superstation (31.09°N, 120.98°E) in Qingpu District, Shanghai, situated in the southwestern suburban region (**Figure S1**). The site is proximal to Jiangsu and Zhejiang Provinces and frequently impacted by regional transport. The surrounding landscape is characterized by vegetation, residential areas, and scattered industrial facilities, with a major traffic corridor approximately 600 m southeast of the station. The observation period spanned from November 1 to December 31, 2024.

2.2 Instrumentation

SPAMS was utilized for real-time chemical analysis of individual particles, effectively analyzing particles with aerodynamic diameters (Dp) from 0.2 to 2 μm at high temporal resolution. Details regarding the SPAMS (Hexin Analytical Instrument Co., Ltd., China) have been reported by previous studies(Lian et al., 2025; Li et al., 2011). Briefly, ambient aerosols were drawn through a ~100 μm critical orifice into an aerodynamic lens, where the particles were accelerated and focused along the centerline. In the sizing region, particles traversed two 532 nm continuous lasers separated by 6 cm. The time-of-flight between the two photomultiplier signals was used to determine particle velocity, which was then calibrated to particle size using polystyrene latex standards. Particle ionization was triggered based on velocity using a 266 nm Nd: YAG laser (1.0 mJ) at the ion source center, generating both positive and negative ions that were analyzed by a time-of-flight mass spectrometer. Due to the potential suppression of negative ions by water vapor, only particles exhibiting both positive and negative ion spectrum (MASS mode) were considered in this study.

The complementary online measurements included the MARGA ADI 2080 for hourly monitoring of water-soluble inorganic ions (NH_4^+, Na^+, K^+, Ca^{2+}, Mg^{2+}, Cl^-, NO_3^-, SO_4^{2-}) and trace gases (NH_3, HNO_2, HNO_3, HCl, SO_2). The Xact 625 was used for hourly quantification of $PM_{2.5}$ metal elements (Si, Fe, Ca, Zn, Mn, Pb, Ba, Cu, Cd, As, Cr, Se). $PM_{2.5}$ and PM_{10} mass concentrations were measured using a tapered element oscillating microbalance. Ozone (O_3), nitrogen oxides (NOx), sulfur dioxide (SO_2), and carbon monoxide were monitored by UV photometry, chemiluminescence, pulsed fluorescence, and non-dispersive IR, respectively. Additionally, a Thermal-optical carbon analyzer (DRI 2001) was employed to measure organic carbon (OC) and elemental carbon (EC) via temperature-programmed analysis.

2.3 SPAMS data analysis

The single-particle size and chemistry data were processed using the COCO toolbox (MATLAB 2014b; MathWorks, Inc.). The Art-2a core clustering algorithm performed self-organizing classification based on ion-peak composition and intensity, with parameters set to a vigilance factor of 0.8, a learning rate of 0.05, and 20 iterations. Despite the 0.8 threshold producing numerous clusters, the initial classes were merged by expert rules considering spectral features and temporal behavior. Sodium ($^{23}Na^+$) and potassium ($^{39}K^+$), to which the SPAMS instrument is highly sensitive, were excluded as primary markers during

https://doi.org/10.5194/egusphere-2026-2447
Preprint. Discussion started: 3 July 2026

the manual merging process. Class names indicate the dominant ions or likely sources but do not represent the complete particle composition. A total of 4,893,140 particles with both positive and negative spectra were collected in autumn-winter period of 2024, achieving a hit efficiency of 18.9% (MASS/SIZE × 100%). The number concentration closely followed $PM_{2.5}$ mass variations over time, demonstrating that SPAMS effectively captured local variability in $PM_{2.5}$ (**Figure S2**).

2.4 Semi-quantitative optimization for SPAMS

We employed a multiple linear regression (MLR) approach to couple single-particle data from a SPAMS instrument with bulk measurements of water-soluble ions (MARGA), metals (XRF), and organic/elemental carbon (OC/EC, DRI-2001). The resulting fitted equation was as follows.

$$[NO_3^-] = -406.353 - 6.387\times10^{-7}\times ANO_3 + 0.462\times[PM_{2.5}] + 7.174\times10^{-5}\times NPM_{2.5} + 0.356\times T + 0.532\times TP + 0.254\times WS + 0.038\times RH + 0.386\times P \quad (R=0.68)$$

The nitrate mass concentration ($[NO_3^-]$, μg/m^3) is related to the SPAMS nitrate peak area (ANO_3, a.u.), $PM_{2.5}$ mass concentration ($[PM_{2.5}]$, μg/m^3), and particle number ($NPM_{2.5}$, cm^{-3}). Meteorological variables include temperature (T, °C), total precipitation (TP, mm), wind speed (WS, m/s), relative humidity (RH, %), and pressure (P, hPa). These predictors were selected based on their physical relevance to nitrate loading, SPAMS detection response, aerosol abundance, and meteorological influences on nitrate formation and sampling conditions. In the final regression model, all retained predictors were statistically significant ($p < .001$), indicating measurable associations with nitrate mass concentration. Therefore, the MLR model was used as a semi-quantitative mass-constrained correction rather than as a direct mechanistic model. Detailed descriptions of semi-quantitative methods can be found in **Supplement S1**. The model demonstrated a correlation coefficient of R = 0.68, with all predictors being statistically significant ($p < .001$). Estimating sampling efficiency as the ratio of $PM_{2.5}$ number to $PM_{2.5}$ mass did not significantly affect R for either linear or machine-learning models. No notable logarithmic or exponential nonlinearity was observed, and sampling efficiency showed no significant correlation with humidity. This framework effectively combines instrument response, $PM_{2.5}$ levels, and meteorological data, enabling quantitative correction of SPAMS data for environmental applications.

2.5 Source apportionment coupling single particle

For the autumn-winter period of 2024, nitrate-containing particles were categorized into four major classes and 12 subclasses through manual consolidation of Art-2a results (**Supplement S2; Table S1**). This process preserved particle types representing 95% of nitrate-containing particles (K_CN indicates concurrent K, C, and N signatures in nitrate particles). The bulk nitrate mass was initially assigned to individual particles based on peak area and subsequently distributed among subclasses by number fraction. The relationships between bulk nitrate and various metrics were examined through regression analyses. To maintain statistical robustness, zero counts were adjusted to 0.1 cm^{-3}, and negative values post-allocation were omitted. The bulk and SPAMS datasets were then synchronized to form a non-negative matrix for source apportionment using non-negative

https://doi.org/10.5194/egusphere-2026-2447
Preprint. Discussion started: 3 July 2026

matrix factorization (NMF; R package "NMF"). Results based on (i) bulk species and (ii) nitrate-particle-only inputs were compared and cross-verified (**Supplement S3**).

2.6 Backward trajectory clustering and regional transport analysis

To identify the dominant air-mass transport pathways affecting the sampling site, 24-h backward trajectories were calculated using the HYSPLIT 4 model (Hybrid Single-Particle Lagrangian Integrated Trajectory) driven by GDAS (1° × 1°) meteorological fields. The trajectories started every hour at an arrival height of 500 m a.g.l., representing the average boundary-layer height at the observation site. The computed trajectory endpoints were converted into ESRI PolylineZ shapefiles and imported into the TrajStat plugin integrated within the MeteoInfo GIS platform(Wang et al., 2009). Cluster analysis was performed in TrajStat to group air-mass trajectories with similar transport patterns. The angle-distance method was selected as the similarity metric because it effectively preserves directional information of the trajectories(Li et al., 2020). The hierarchical agglomerative algorithm (Ward's minimum-variance method) was applied to minimize the intra-cluster variance during merging. For each cluster, the software generated mean trajectories, spatial deviation envelopes, and frequency statistics (% of total trajectories). Each trajectory was assigned to the nearest cluster centroid based on the minimum angular distance. The resulting clusters were visualized with color-coded mean-trajectory maps, and their relative frequencies were used to evaluate the dominant air-mass pathways during different pollution episodes (PE1–PE4).

3 Results and Discussion

3.1 Variation of nitrate-containing particle classes

The nitrate-containing particles were classified into four categories: NO_3Lv1, NO_3Lv2, NO_3Lv3, and NO_3Lv4. NO_3Lv1–NO_3Lv4 represent a progressive transition in the chemical characteristics of nitrate-containing particles. NO_3Lv1 and NO_3Lv2 are characterized by relatively stronger sulfate-related signals and weaker nitrate signals, suggesting sulfate-rich nitrate-containing particles or particles at an earlier stage of nitrate enrichment. NO_3Lv3 and NO_3Lv4 exhibit stronger nitrate fragment ions, especially NO_2^- and NO_3^-, and relatively weaker sulfate signals, indicating more nitrate-rich and more processed particles. Among them, NO_3Lv4 shows the strongest nitrate signals, the highest number contribution, and a pronounced accumulation-mode distribution, suggesting that it represents the most nitrate-enriched and aged particle class during the observation period. The averaged relative mass spectra (**Figure 1**) consistently exhibit distinct ion signatures. In the positive spectra, NO_3Lv1 and NO_3Lv2 show a strong $39K^+$ presence, accompanied by $23Na^+$ and C_3H^+. The negative spectra display a dominant $97HSO_4^-$, while $16O^-$, $35/37Cl^-$, $79PO_3^-$, and $46NO_2^-/62NO_3^-$ are less prominent, with NO_3Lv2 having higher 46/62 ratios than NO_3Lv1. Similarly, NO_3Lv3 and NO_3Lv4 exhibit strong $39K^+$ in the positive spectra. In the negative spectra, $46NO_2^-/62NO_3^-$ are more pronounced, and $97HSO_4^-$ is relatively weaker, with NO_3Lv4 showing the strongest 46/62 signatures.

https://doi.org/10.5194/egusphere-2026-2447
Preprint. Discussion started: 3 July 2026

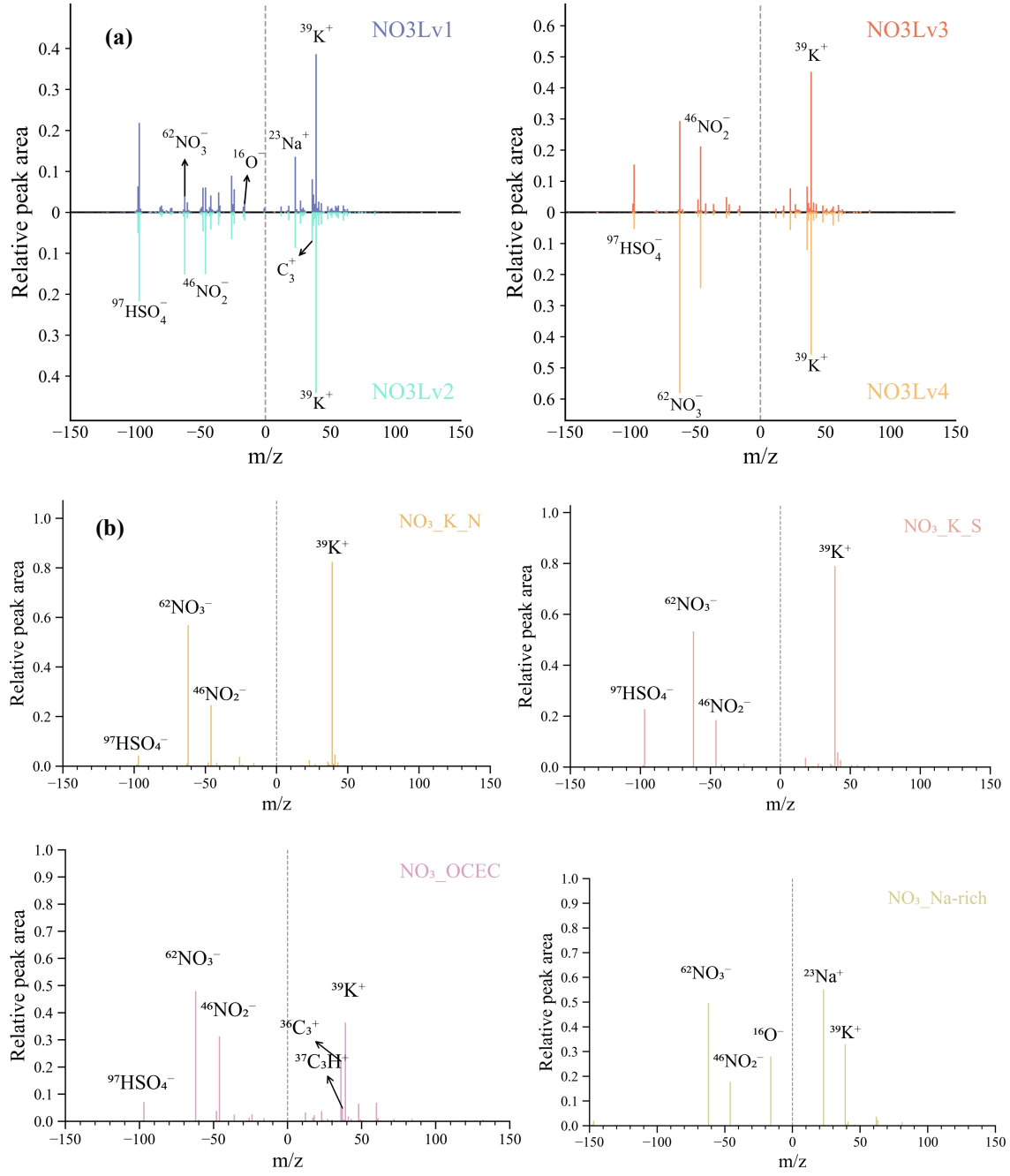

Figure 1: The average single-particle mass spectra for (a) four nitrate-containing particle classes (NO_3Lv1, NO_3Lv2, NO_3Lv3, and NO_3Lv4), and (b) nitrate-containing particle types (NO_3_K_N, NO_3_K_S, NO_3_OC/EC, and O_3_Na-rich) derived from NO_3Lv4 cluster analysis. The x-axis is the mass-to-charge ratio (m/z), and the y-axis is the relative peak area (normalized intensity). Positive values correspond to cation signals and negative values to anion signals, indicating the relative

https://doi.org/10.5194/egusphere-2026-2447
Preprint. Discussion started: 3 July 2026

importance of each ion within that particle type. Characteristic marker ions are labeled, including K^+ (m/z 39), Na^+ (m/z 23), organic fragment ions such as $C_3H^+$and C_3^+, and anions such as NO_3^- (m/z 62), NO_2^- (m/z 46), and HSO_4^- (m/z 97).

Cross-correlations among nitrate classes revealed stronger links within the NO_3Lv1–NO_3Lv2 and NO_3Lv3–NO_3Lv4 (e.g., 0.65 / 0.7647 and 0.5418 / 0.6579 for mass concentration / number, respectively), indicating shared sources and formation pathways. NO_3Lv1 displayed weak correlations with NO_3Lv3–NO_3Lv4 (e.g., with NO_3Lv4, 0.018 for mass concentration and 0.0773 for number), implying different physicochemical properties or formation pathways (**Figure S11**).

The four nitrate-containing particle classes (NO_3Lv1–NO_3Lv4) each exhibited distinct diurnal patterns in their number and mass concentrations (**Figure 2**). NO_3Lv1–NO_3Lv3 all show strong daytime enhancements in both number and mass concentrations, with concentrations generally rising in the morning (around 08:00) and peaking during the early afternoon (~12:00–16:00)(Tao et al., 2023; Tian et al., 2025). Such daytime peaks are attributable to increased secondary nitrate formation driven by daytime photochemistry and morning emissions. For example, field observations in urban China have reported that particulate nitrate levels climb through the morning and reach a maximum at midday or early afternoon due to photochemical production of HNO_3 and ample NH_3 availability[26]. Among them, NO_3Lv3 shows the most pronounced bimodal number peak, likely influenced by both morning traffic emissions and midday photochemical formation. NO_3Lv2 and NO_3Lv3 share similar size distributions centered at 0.5–0.7 μm, aligning with typical accumulation-mode secondary nitrate from regional transport and aging processes. Studies of aged, regionally transported aerosol in polluted environments have found that submicron nitrate tends to be internally mixed and highly aged, with mass distribution maxima around 0.6–0.8 μm(Li et al., 2021a). NO_3Lv1, in contrast, displays a broader and more variable size distribution peaking around 0.3 μm, indicating fresh, fine-mode particles that may result from local combustion emissions or early-stage secondary formation. This class shows the weakest mass response during the day, consistent with a smaller particle size and lower average mass per particle.

NO_3Lv4, which represents more polluted or aged aerosol conditions, shows a markedly different diurnal behavior. Its number concentration remains relatively flat throughout the day (indicating that the particle count does not vary as strongly diurnally), but its mass concentration exhibits a pronounced midday dip. Specifically, NO_3Lv4 mass tends to be highest during the early morning and late evening, while dropping around midday. This pattern is consistent with the accumulation of large, aged nitrate particles under a stable nocturnal boundary layer at night and in the morning, followed by partial dispersion or evaporation when the boundary layer rises and temperature increases at midday. The size distribution of NO_3Lv4 particles also peaks in the accumulation-mode (~0.5–0.7 μm, like NO_3Lv2/Lv3); however, a distinguishing feature is that NO_3Lv4 shows significant coarse-mode enrichment (>1 μm), especially in NaK and K_N. The description of size distribution can refer to sect.3.3.

https://doi.org/10.5194/egusphere-2026-2447
Preprint. Discussion started: 3 July 2026

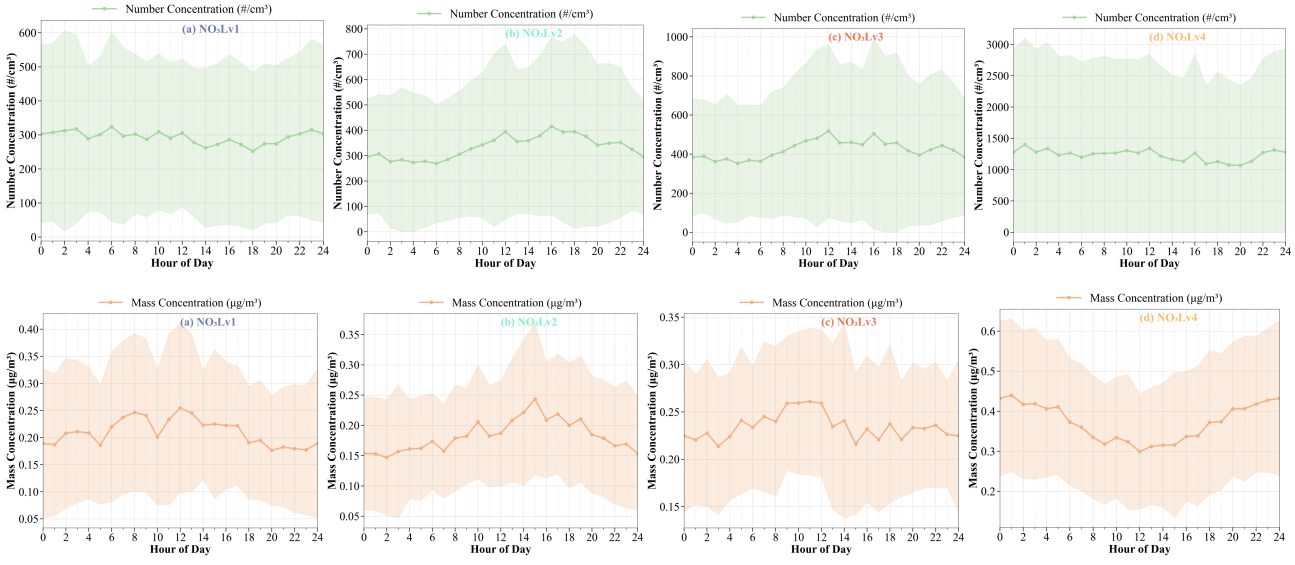

Figure 2: Diurnal patterns of number concentrations and mass concentrations for four nitrate-containing particle classes. The solid line shows the average value as a function of local time (Hour of Day, 0–24 h), and the shaded area represents the variability (25th and 75th percentiles).

NO_3Lv4 class dominated both the mass concentration proportion (40.1%) and number-contribution (53.7%) metrics, suggesting high particle counts and larger per-particle nitrate levels for this class (**Figure 3**). NO_3Lv2 class contributed 18.0% of the mass concentrations and 14.8% of the number, which was followed by NO_3Lv4 class. The differences in both proportions from NO_3Lv1 to NO_3Lv4 are likely to reflect differences in source and formation processes among the nitrate classes.

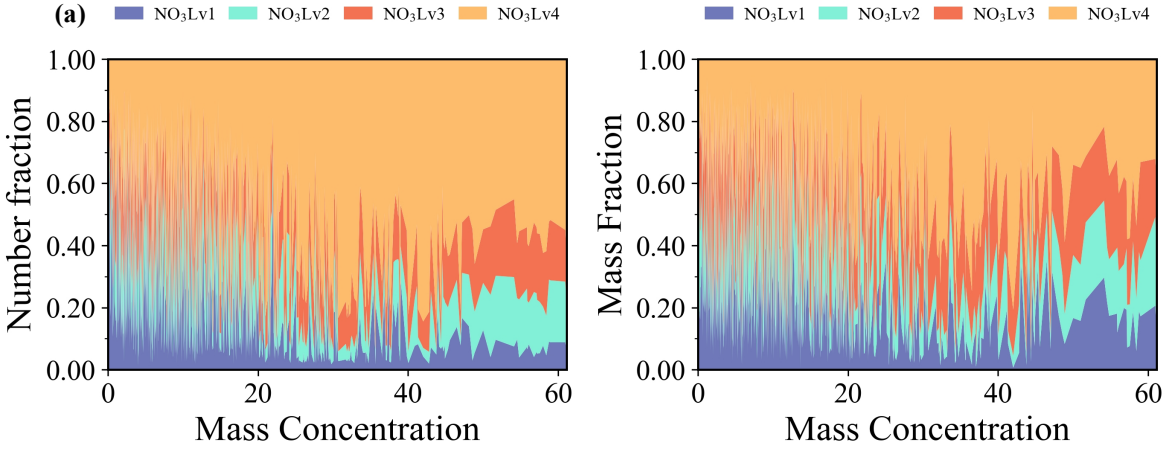

https://doi.org/10.5194/egusphere-2026-2447
Preprint. Discussion started: 3 July 2026

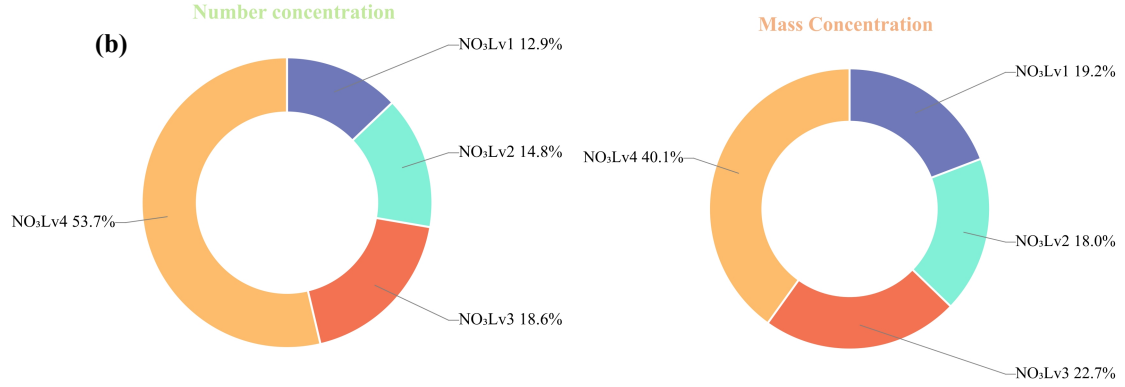

Figure 3: (a) The variation of number concentrations and mass concentrations for four nitrate-containing particle classes as a function of nitrate mass concentration during the whole observation period. (b) The average fractions of four nitrate-containing particle classes in number concentrations and mass concentrations.

Across the full nitrate concentration range, NO_3Lv4 is persistently the dominant class (**Figure 3a**). Its number fraction remains highest at most loadings and generally increases with nitrate mass concentration, indicating progressive enrichment of NO_3Lv4 class as pollution intensifies. At elevated nitrate mass concentrations, intermittent enhancements of NO_3Lv3 (and, to a lesser extent, NO_3Lv2) are evident, while NO_3Lv1 contributes only a minor share throughout. In mass space **(Figure 3)**, NO_3Lv4 also accounts for the largest share, although its mass fraction is typically lower than its number fraction, consistent with differences between particle counts and peak-area–weighted contributions. The rise of NO_3Lv1, NO_3Lv3 at higher loadings (Nitrate Mass >45) is more visible in the mass fractions, reflecting their larger peak-area signals when these classes are present. Overall, both panels demonstrate NO_3Lv4 dominating the particle number and mass loadings.

3.2 Variation characteristics of the chemical composition of nitrate-containing particles

Utilizing a combination of Art-2a and manual consolidation, nitrate-containing particles observed during the autumn-winter period of 2024 were classified into 12 distinct types, including elemental carbon (NO_3_EC), organic carbon (NO_3_OC), a mixture of organic and elemental carbon (NO_3_OCEC), ammonium (NO_3_Ammonium), potassium-nitrate (NO_3_K_N), potassium-carbon-nitrogen-nitrate (NO_3_K_CN), potassium-sulfate (NO_3_K_S), sodium-potassium (NO_3_NaK), sea salt-(NO_3_Na-rich), dust (NO_3_Dust), Fe-rich particles (NO_3_Fe), and other types (NO_3_Other). Representative relative peak-area mass spectra were generated for the four nitrate classes. During manual consolidation, only particle types representing the top 95% of nitrate-containing particles were retained. The distribution of types across the four nitrate classes is detailed in **Table S1**.

We present the characteristics of NO_3_K_N, NO_3_K_S, NO_3_OCEC, and NO_3_Na-rich in NO_3Lv4 (**Figure 1 and Figure S12**). NO_3_K_N and NO_3_K_S both show strong $39K^+$ and nitrate fragments at $46NO_2^-$ and $62NO_3^-$, but N_{O3}_K_S exhibits a more evident $97HSO_4^-$ signal than NO3_K_N, suggesting a stronger sulfate-related feature. Ammonium displays strong $18NH_4^+$ and $39K^+$ (positive) and $62NO_3^-$ (negative) with weaker $46NO_2^-$ and $97HSO_4^-$. NO_3_Na-rich is characterized by strong $23Na^+$ and

https://doi.org/10.5194/egusphere-2026-2447
Preprint. Discussion started: 3 July 2026

$39K^+$ in the positive spectra, together with abundant nitrate fragments, including 46 NO_2^- and $62NO_3^-$, and a strong $16O^-$ signal in the negative spectra. EC is characterized by strong $36C_3^+$ and $39K^+$ (positive) and a dominant $62NO_3^-$ (negative) with weaker $46NO_2^-$ and $97HSO_4^-$. Fe is noted for strong $56Fe^+$ (positive) with weak $39K^+$ and strong 46/62 nitrate and weak $97HSO_4^-$ (negative). The observed enrichment of K^+ as a marker for biomass-burning particles and the chloride–nitrate replacement in aged sea-salt particles is consistent with previous single-particle and heterogeneous-chemistry studies(Krueger et al., 2003; Liu et al., 2022).

Figure 4 illustrates that NO_3_EC significantly contributes to all classes (23.8%–38.8%), highlighting a widespread combustion influence. NO_3Lv1 is enriched with NO_3_EC (25.7%) and OC (18.3%), indicating substantial organic aerosol impacts. NO_3Lv2 (NO_3_EC / NO_3_OC / NO_3_OCEC = 23.8%/18.2%/11.7%) reflects pronounced primary combustion signatures. NO_3Lv3 shows elevated levels of NO_3_NaK (17.4%), suggesting contributions from seasalt. NO_3Lv4, with the highest NO_3_EC (38.8%) and NO_3_K_N (18.4%), suggests enhanced combustion and secondary nitrate formation. The observed EC–nitrate co-mixing in polluted conditions aligns with urban findings in central and eastern China(Zhou et al., 2022). The observed EC-nitrate association may be attributed to two complementary processes. First, EC-containing particles are closely related to combustion emissions, including traffic and biomass or coal combustion, which can be accompanied by NOx emissions and thus provide precursors for nitrate formation. This common-source influence can partly explain the frequent coexistence of EC and nitrate during pollution episodes. Second, pre-existing EC-containing particles can serve as surfaces or cores for the condensation of HNO_3/NH_4NO_3 or for heterogeneous nitrate formation under high-RH and stagnant conditions. Therefore, EC-nitrate particles likely reflect the combined effects of primary combustion emissions and secondary nitrate accumulation during atmospheric aging.

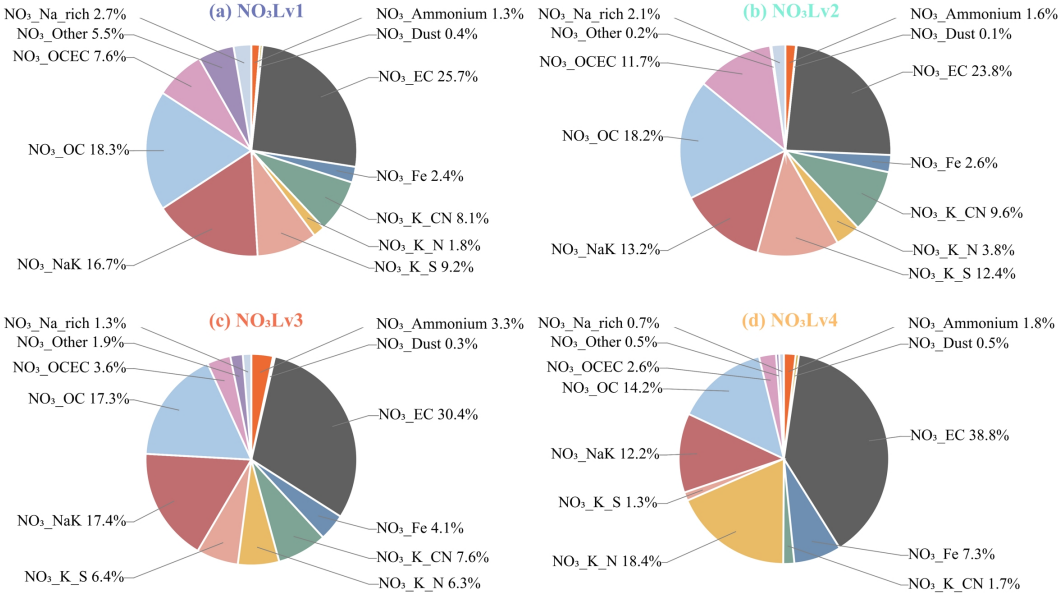

Figure 4: The average fraction of 12 distinct types in total mass of four nitrate-containing particle classes.

https://doi.org/10.5194/egusphere-2026-2447
Preprint. Discussion started: 3 July 2026

The progressive decline in NO_3_OC coupled with the concomitant increase in NO_3_K_N from NO_3Lv1 to NO_3Lv4 suggests an accelerated formation and aging of secondary nitrate under high RH and oxidizing conditions characteristic of the autumn-winter period over the Yangtze River Delta region(Zang et al., 2022).

The temporal dynamics of NO_3_Na-rich concentrations exhibit a distinct seasonal pattern (**Figures. 11-12**). NO_3_Na-rich peaks are observed in November, followed by significant declines in both abundance and fractional contribution in December. This pattern may reflect changes in sodium-rich particle influences and nitrate aging processes, potentially affected by autumn southeasterly air masses (Chen et al., 2016). Additionally, the increase in NO_3Lv2–Lv4 in December further reduces the relative fraction of seasalt.

3.3 Size distribution of nitrate-containing particles

The three classes NO_3Lv2, NO_3Lv3, and NO_3Lv4 exhibit highly similar size patterns, all peaking at 0.5–0.7 μm, suggesting comparable secondary formation and aging processes (**Figure S15**). In contrast, NO_3Lv1 displays a distinct peak at ~0.3 μm with a broader distribution across 0.3–2.0 μm, implying different sources or formation pathways. All classes are concentrated in the submicron mode (<1 μm), consistent with the predominance of secondary nitrate formation. This finding corroborates previous observations showing that ammonium nitrate typically dominates the accumulation mode (~0.5–0.7 μm) in wintertime urban and regionally influenced air(Cheng et al., 2018).

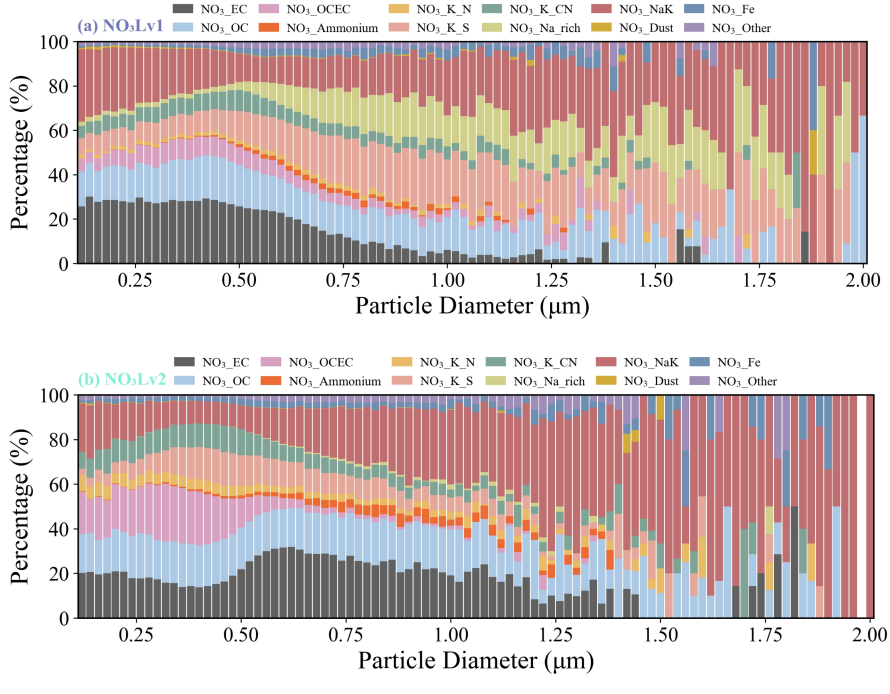

https://doi.org/10.5194/egusphere-2026-2447
Preprint. Discussion started: 3 July 2026

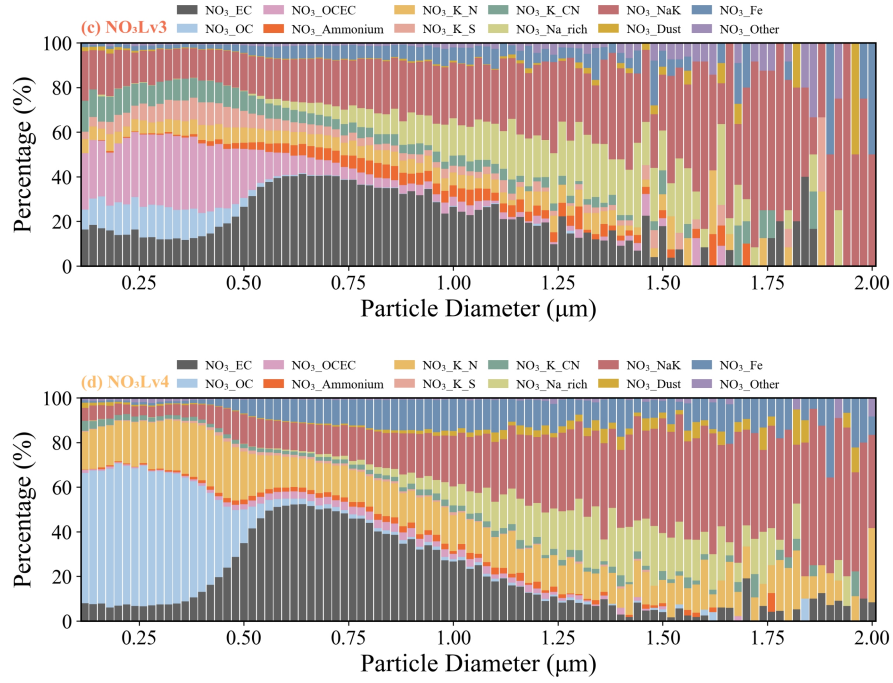

Figure 5: Size-resolved source contributions of nitrate-containing particle classes. Stacked bar charts show the fractional contribution of different nitrate types as a function of particle diameter for (a) NO_3Lv1, (b) NO_3Lv2, (c) NO_3Lv3, and (d) NO_3Lv4. Each color denotes a specific nitrate-containing particle type, including elemental carbon (NO_3_EC), organic carbon (NO_3_OC), organic/elemental carbon (NO_3_OCEC), ammonium (NO_3_Ammonium), potassium from different source signatures (NO_3_K_N, NO_3_K_S, NO_3_K_CN, NO_3_NaK), sodium-rich nitrate-containing particles (NO_3_Na-rich), dust (NO_3_Dust), Fe-rich particles (NO_3_Fe), and other types (NO_3_Other).

In NO_3Lv1, NO_3_EC, NO_3_OCEC, and NO_3_OC were concentrated in fine mode (<0.5 μm), whereas NO_3_Na-rich and NO_3_K_S appear in the large mode (>0.5 μm) (**Figure 5**). The size distribution implies that NO_3Lv1 largely externally mixed primary emissions. This is consistent with its diurnal variations. Field studies have noted that while freshly emitted carbon tends to be ultrafine, in a heavily polluted air mass the mass median of carbonaceous particles can shift up into the 0.2–1.0 μm range(Herner et al., 2006).

NO_3Lv2 is dominated by NO_3_EC and NO_3_NaK, with the fraction of NO_3_NaK steadily increasing at >0.75 μm, while NO_3_EC remains relatively stable within 0.5–0.75 μm. NO_3_K_S and NO_3_OCEC exhibited significant distributions in the small particle size range (<0.5 μm). NO_3_OC showed a stable distribution proportion in whole size. For NO_3Lv3, NO_3_NaK is more uniformly distributed, NO_3_EC peaks 0.5~0.75 μm and declines with size, and NO_3_OC and NO_3_OCEC ~~is~~are largely confined to <0.5 μm. The NO_3_Na-rich fraction grows steadily with particle size above ~0.75 μm, indicating that sodium-rich nitrate-containing particles are preferentially enriched in larger particles. In NO_3Lv3, a significant portion of NO_3_OC likely comes from secondary formation or aged primary organic matter, which typically yields particles in the low size range. Thus,

https://doi.org/10.5194/egusphere-2026-2447
Preprint. Discussion started: 3 July 2026

OC continues to dominate the smaller end of the size distribution and does not substantially extend into the coarse mode. It indicates that primary aerosol sources are being modified by secondary accumulation from regional transport and aging processes for NO_3Lv2 and NO_3Lv3.

The particle size distribution characteristics of NO_3Lv4 differ significantly from those of NO_3Lv1- NO_3Lv3 .For NO_3Lv4, a distinct size-dependent partitioning emerges: NO_3_K_N and NO_3_OC dominate the fine mode (<0.5 μm), together accounting for over 60% of the particle mass, whereas NO_3_EC and NO_3_NaK strengthen at >0.5 μm, with NO_3_NaK averaging ~30% at 0.8–1.5 μm, indicative of coarse-mode enrichment. High NO_3_K_N proportion within the large particle size range represents an advanced state of aerosol aging during the nighttime (Diurnal Patterns; **Figure 2**) where even the coarse fraction is influenced by secondary inorganic formation. In addition to its strong nitrate signals and dominant contribution, the size-resolved distribution further supports the aged and secondary-processed nature of NO_3Lv4. Its size distribution mainly peaked at 0.5–0.7 μm, which is consistent with accumulation-mode secondary nitrate formed through gas-particle partitioning and heterogeneous processing. Moreover, the relatively high fractions of K-rich nitrate-containing particles and Na-rich nitrate-containing particles suggest that secondary nitrate may have accumulated on pre-existing combustion-related particles and aged Na-containing particles. These spectral, size-resolved, and mixing-state features jointly indicate that NO_3Lv4 represents the most nitrate-enriched and atmospherically processed particle class during the campaign.

The larger size range (>0.5 μm) in NO_3Lv1–NO_3Lv4 showed enhanced contributions from sodium-/potassium-rich nitrate-containing particles, especially NO_3_NaK and NO_3_Na-rich. This size-dependent pattern suggests that larger particles provided important surfaces or matrices for nitrate accumulation and aging. In NO_3Lv1, NO_3_NaK is predominantly found in the fine mode (<0.5 μm), with the decrease in its relative fraction in the coarse mode (>0.5 μm), a little bit different from other three NO_3 classes (**Figure S16**). Sea-salt particles originate from ocean spray and naturally occur at larger sizes – indeed, most of their mass is in the super-micron range (coarse mode)(Jensen and Nugent, 2017). These patterns indicate size-dependent shifts in the relative importance of secondary nitrate accumulation compared to the aging of primary/sea-salt/dust sources across different pollution stages. The replacement of chloride with nitrate in sea-salt particles, resulting in $NaNO_3$ formation, aligns with evidence from single-particle analyses and heterogeneous chemistry(Gard et al., 1998).

3.4 Source variations in typical pollution processes

To clarify sources and their contributions, the NMF analysis was used to resolve the sources of nitrate-containing particles. Seven factors (N1–N7) corresponding to combustion, dust, non-ammonium secondary inorganic aerosol (SIA), industrial sources, sea-salt, ammonium-nitrate SIA, and mixed nitrate–Na-rich factor were identified. The factor profiles, time series, and diurnal variations provide insights into the dominant chemical signatures and temporal behavior of each source (**Figure S8a and Figure 6a**).

https://doi.org/10.5194/egusphere-2026-2447
Preprint. Discussion started: 3 July 2026

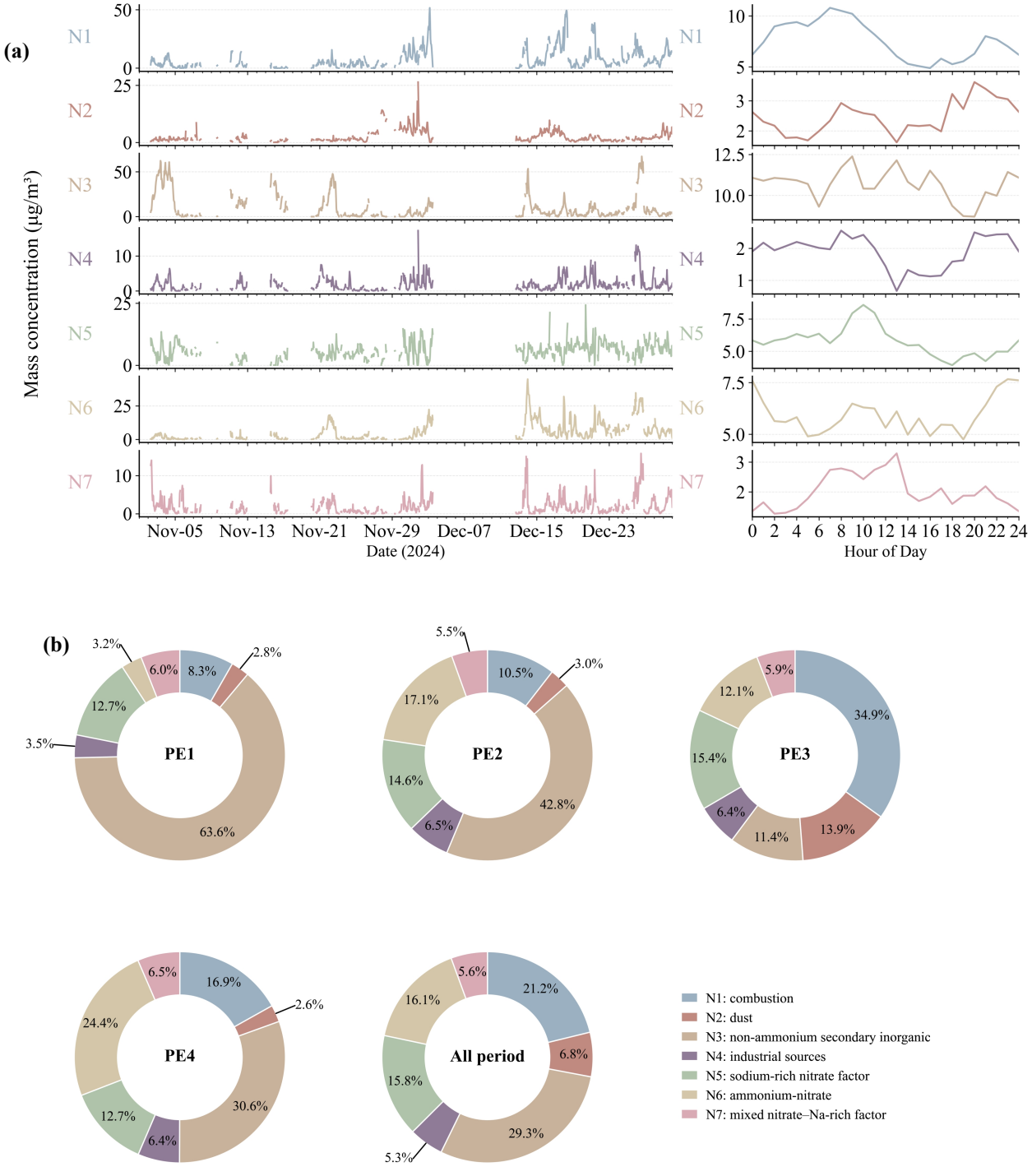

315 **Figure 6: (a) Time series (left) and diurnal profiles (right) of mass concentration for seven nitrate-related source factors (N1–N7) resolved over the full observation period. (b) Source contribution of N1–N7 factors to total particulate nitrate**

https://doi.org/10.5194/egusphere-2026-2447
Preprint. Discussion started: 3 July 2026

during four pollution episodes and the entire campaign. The factors are interpreted as: N1 – combustion-related nitrate, N2 – dust-related nitrate, N3 – non-ammonium secondary inorganic aerosol, N4 – industrial sources, N5 – sodium-rich nitrate factor, N6 – ammonium-nitrate, and N7 – mixed nitrate–Na-rich factor.

N1 (Combustion source) exhibited strong EC, OC, and K fragments (**Figure S8a**), indicating mixed contributions from traffic and biomass burning. Its time series showed sharp morning and nighttime peaks, reflecting local accumulation under low boundary-layer conditions. N2 (Dust source) was enriched in Ca, Fe, and Si, consistent with resuspended road dust or regional crustal transport, and showed weak diurnal variability. N3 (Secondary inorganic aerosol – non-ammonium nitrate) displayed dominant NO_3^- signals with NO_3_Fe, NO_3_other enrichment, suggesting formation of non-ammonium nitrates through heterogeneous neutralization. The factor increased at night and during regional transport events. N4 (Industrial source) showed high fractions of metallic ions (Fe, Pb, Zn, Mn, Cu), indicative of metallurgical and industrial combustion emissions, with daytime maxima corresponding to active operations. N5 (sodium-rich nitrate factor) was characterized by sodium-rich particle signatures and nitrate-related fragments, indicating nitrate aging of Na-rich particles. N6 (Secondary inorganic aerosol – ammonium nitrate) was dominated by NO_3 and NH_4, pointing to homogeneous gas-particle partitioning of HNO_3 and NH_3 under cold and humid conditions. N7 (mixed nitrate–Na-rich factor) exhibited concurrent NO_3_Na-rich particles and depleted Cl^-, suggesting nitrate aging of Na-rich particles, potentially involving chloride displacement.

Several pollution episodes (PEs) were detected during the campaign, highlighted by shaded intervals. During PE1 (2–5 November 2024), NO_3_EC peaked at ~10 μg m^{-3}, followed by NO_3_Na-rich (**Figure S13**). Concurrently, N3 (Secondary inorganic aerosol – non-ammonium nitrate), N5(sodium-rich nitrate factor), and N7(mixed nitrate–Na-rich factor) increased. On 3–4 November, TC reached a local maximum while nitrate continued to rise, indicating the presence of primary carbonaceous emissions and secondary nitrate formation. **Figure 7** shows five major air mass clusters arriving at Shanghai. The dominant cluster (red, 27.08%) originated from northern China, passing over the Bohai and Yellow Seas, indicating long-range transport from the North China Plain. The blue and cyan clusters (8.33% and 4.17%) were associated with maritime trajectories from the Yellow Sea, while the green cluster (10.42%) represented short-range transport from nearby inland regions such as Jiangsu and Anhui. The minor pink cluster (2.08%) corresponded to local circulation patterns. The dominant PE1 clusters advected from the North China Plain across the Bohai and Yellow Seas, consistent with enhanced secondary inorganic aerosol in the form of non-ammonium nitrate. The transport pathway across the Bohai and Yellow Seas may have contributed to the transport and aging of sodium-rich particles along mixed continental–marine pathways.

Starting 20 November, secondary nitrate aerosol (N3 and N6) levels rose for three days, peaking around 22 November (PE2), with the NO_3_EC decreasing (**Figure S13**). The trajectories are predominantly directed from the north and northeast, with the majority passing over Shandong Province and the Yellow Sea before arriving in Shanghai. The dominant clusters (green and yellow) indicate frequent air mass transport from northern Jiangsu and Shandong regions, consistent with cold-season northerly flows. The PE2 clusters, characterized by air masses transported from the Shandong and northern Jiangsu across the Yellow Sea, corresponded to simultaneous increases in both ammonium nitrate N6 and non-ammonium nitrate components N3. This pattern suggests that the air masses carried substantial precursors (NO_x, NH_3) from northern inland source regions, favoring

https://doi.org/10.5194/egusphere-2026-2447
Preprint. Discussion started: 3 July 2026

the formation of ammonium nitrate under low-temperature and high-humidity conditions, while sodium-rich particles and dust-related components transported along mixed continental–marine pathways may have provided reactive surfaces or alkaline matrices for heterogeneous reactions, facilitating the conversion of acidic gases, such as HNO_3 and N_2O_5, into non-ammonium nitrate. The increase in secondary inorganic aerosol factors during nighttime and polluted periods, together with the dominance of nitrate-rich NO_3Lv4 particles and their accumulation-mode size distribution, suggests active secondary nitrate formation under stagnant and humid conditions. Because NO_3 and N_2O_5 were not directly measured in this study, we interpret the nighttime enhancement of nitrate-related factors and the high-RH conditions during pollution episodes as indirect evidence that nocturnal heterogeneous nitrate production may have contributed to nitrate accumulation. Therefore, the enhancement of total secondary inorganic aerosol during PE2 is attributed to both homogeneous gas-particle partitioning and heterogeneous reactions along the mixed continental–marine transport pathways. It is consistent with the increased nocturnal NO_3/N_2O_5 chemistry and high-RH heterogeneous production characteristic of winter pollution episodes.

During the period of November 29 to December 4 (PE3), the concentrations of EC-nitrate initially increased, while NO_3_OC and NO_3_K_N decreased. Combustion N1 and dust N2 continued to rise, peaking around December 2. Most trajectories are confined within the Yangtze River Delta region, suggesting limited long-range transport. The major clusters indicate local and regional circulation patterns, with air masses primarily originating from nearby provinces such as Jiangsu, Anhui, and Zhejiang. This pattern is characteristic of stagnant meteorological conditions conducive to pollutant accumulation. Additionally, clusters originating from long-distance transport in the northwest regions of Henan and Shanxi suggest that this pollution process is also little accompanied by aging characteristics.

During PE4 (23–27 December), concentrations of N3/N4/N6/N7 steadily increased, peaking on 26–27 December, with TC tracking N4. PE4 exhibits continental pathways from the North China Plain and northern Jiangsu, pointing to regional transport of industrial-derived pollutants and secondary inorganic aerosol formed from inland industrial and urban regions. Under stagnant and shallow boundary-layer conditions with cold and humid weather, local primary emissions accumulated, while reactions between NOx and NH_3, together with nocturnal heterogeneous uptake of N_2O_5, likely accelerated the formation of ammonium nitrate. Therefore, PE4 represents a compound pollution event driven by both local combustion accumulation and regional nitrate inflow, consistent with the widespread wintertime enhancement of nitrate observed across eastern China.

https://doi.org/10.5194/egusphere-2026-2447
Preprint. Discussion started: 3 July 2026

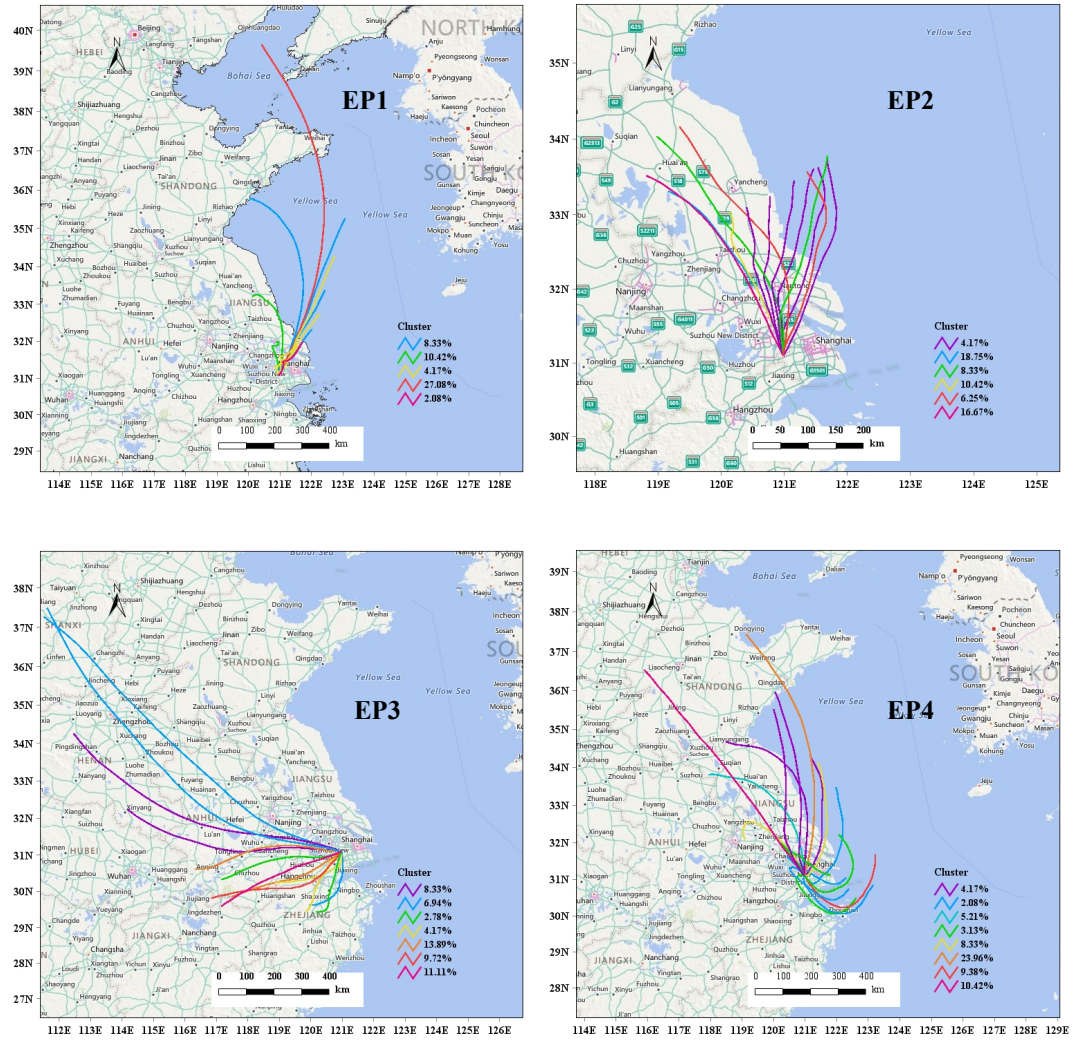

Figure 7: Clustered 24-h backward air mass trajectories during four pollution episodes of the campaign. Each panel shows the transport pathways of air masses arriving at the sampling site, with trajectories grouped into clusters based on similarity in transport direction and origin. Colored lines indicate individual clusters, and the legend in each panel reports the fractional occurrence (%) of each cluster. Backward trajectories were generated using the NOAA HYSPLIT model and clustered using TrajStat. Basemap: © OpenStreetMap contributors.

https://doi.org/10.5194/egusphere-2026-2447
Preprint. Discussion started: 3 July 2026

4 Conclusions and Atmospheric Implications

We conducted an autumn-winter campaign at the Shanghai Dianshan Lake superstation to develop a semi-quantitative framework that integrates SPAMS with bulk measurements and NMF source apportionment. This approach demonstrated that a semi-quantitative SPAMS–NMF workflow can convert single-particle counts and relative ion signals into mass-relevant, source-resolved information on relevant timescales. This finding enables near-real-time, mass-relevant interpretation of single-particle measurements. Observations further showed that nitrate-containing particles were predominantly in the accumulation mode (0.5–0.7 μm). A specific particle class (NO_3Lv4) that related to secondary formation contributed approximately 40% of the total nitrate ion signal (mass concentration) and accounted for over half of all nitrate-containing particles by number, identifying the important role of secondary formation in the wintertime nitrate burden.

Chemically resolved analysis indicated that these nitrate-containing particles often contained internally mixed components. Notably, EC, NaK, and Na-rich particles coexisted with nitrate in many particles. These features point to rapid nitrate formation occurring in simultaneously with the atmospheric aging of primary combustion emissions, and sodium-rich particles. Diurnal variations and pollution-episode analyses further indicate that wintertime nitrate accumulation at the Dianshan Lake site was promoted by low temperature, high relative humidity, stagnant and shallow boundary-layer conditions, abundant precursors, and regional transport. Because NO_3 and N_2O_5 were not directly measured in this study, the possible contribution of nocturnal NO_3/N_2O_5 chemistry should be interpreted as an inferred pathway based on the nighttime enhancement of secondary nitrate-related factors, which requires further verification by direct measurements in future studies. During haze episodes, northerly and northeasterly inflows often amplified local nitrate levels by transporting additional aged aerosol into the region. Decomposing single-particle mixing states using NMF factors revealed the co-evolution of combustion-derived and secondary inorganic aerosol components during winter pollution episodes, indicating the need for condition-specific precursor emission controls. For example, joint NOx–NH_3 reductions would be most effective during humid, stagnant nighttime periods when N_2O_5 uptake and gas-to-particle partitioning drive rapid ammonium-nitrate formation. Likewise, targeted controls on combustion sources (e.g., traffic and biomass burning) could reduce EC–nitrate co-mixing, thereby limiting the enhancement of light absorption and the alterations in hygroscopic growth caused by such internally mixed particles. In coastal or mixed continental–marine environments, nitrate aging of sodium-rich particles, potentially involving chloride displacement, may also influence particle size distributions and optical properties. These mixing-state considerations extend to climate and visibility: when black carbon is encapsulated by nitrate, its light absorption can be enhanced, and nitrate's hygroscopic growth increases light scattering. Accounting for these effects is essential for accurately evaluating radiative forcing, visibility degradation, and cloud condensation nuclei (CCN) activation in eastern China's winter haze.

Despite these insights, the representativeness of our results is limited by the single suburban site and the autumn–winter observation campaign. Broader sampling across seasons and urban–rural observations is needed. The semi-quantitative calibration approach also carries uncertainties related to approach itself and particle-type-dependent ionization efficiency of SPAMS. Moreover, NMF factorization solutions are not unique and require interpretation of factor profiles and tracers.

https://doi.org/10.5194/egusphere-2026-2447
Preprint. Discussion started: 3 July 2026

Another limitation is the absence of direct measurements of key species (NO_3, N_2O_5, and $ClNO_2$), which limits a complete mechanistic understanding of nighttime nitrate formation. To further advance the understanding of nitrate aerosols, we recommend conducting multi-season, and multi-site studies across the Yangtze River Delta with an expanded observational scope. This should include direct nocturnal oxidant measurements (NO_3, N_2O_5, $ClNO_2$) alongside aerosol liquid water content and pH; improved SPAMS mass-response calibration and region-specific machine learning models to better translate particle counts into mass; nitrate isotope analyses (δ15N, δ18O) to pinpoint sources and formation pathways; and integrated optical and CCN measurements to quantify how EC–nitrate mixing influences aerosol absorption, hygroscopicity, and cloud activation potential. Coupling these efforts with chemical transport modeling under coordinated NOx–NH_3 emission control scenarios would sharpen forecast accuracy and enable more effective interventions tailored to specific times of day and meteorological conditions during winter nitrate pollution episodes.

Code and data availability

The data and codes used in this study are not publicly available due to institutional restrictions. However, the data supporting the findings of this study are available from the corresponding author upon reasonable request.

Author contributions

Wenfei Zhu: Conceptualization, Data curation, Formal analysis, Methodology, Writing – original draft, Writing - review & editing. Qinghong Wang: Data curation, Methodology. Qingsong Wang: Data curation, Methodology. Jialin Shi: Data curation, Methodology, Formal analysis. Juntao Huo: Data curation, Formal analysis. Mei Li: Conceptualization, Data curation, Formal analysis. Yu Sun: Formal analysis. Jun Chen: Formal analysis. Shengrong Lou: Conceptualization, Data curation, Formal analysis. Hui Chen: Project administration, Conceptualization, Data curation, Formal analysis, Writing - review & editing.

Competing interests

The contact author has declared that none of the authors has any competing interests.

Disclaimer

Copernicus Publications remains neutral with regard to jurisdictional claims made in the text, published maps, institutional affiliations, or any other geographical representation in this paper. While Copernicus Publications makes every effort to include appropriate place names, the final responsibility lies with the authors. Views expressed in the text are those of the authors and do not necessarily reflect the views of the publisher.

https://doi.org/10.5194/egusphere-2026-2447
Preprint. Discussion started: 3 July 2026

Acknowledgements

We express our gratitude to the Shanghai Environmental Monitoring Center, Shanghai for providing the relevant supporting data.

Financial support

This research was supported by the Shanghai Municipal Bureau of Ecology and Environment (Hu Huan Ke [2024] No. 31).

Review statement

The review statement will be added by Copernicus Publications listing the handling editor as well as all contributing referees according to their status anonymous or identified.

References

Chen, Y., Cheng, Y., Ma, N., Wolke, R., Nordmann, S., Schüttauf, S., Ran, L., Wehner, B., Birmili, W., van der Gon, H. A. C. D., Mu, Q., Barthel, S., Spindler, G., Stieger, B., Müller, K., Zheng, G. J., Pöschl, U., Su, H., and Wiedensohler, A.: Sea salt emission, transport and influence on size-segregated nitrate simulation: a case study in northwestern Europe by WRF-Chem, Atmos. Chem. Phys., 16, 12081-12097, 10.5194/acp-16-12081-2016, 2016.

Cheng, C., Huang, Z., Chan, C. K., Chu, Y., Li, M., Zhang, T., Ou, Y., Chen, D., Cheng, P., Li, L., Gao, W., Huang, Z., Huang, B., Fu, Z., and Zhou, Z.: Characteristics and mixing state of amine-containing particles at a rural site in the Pearl River Delta, China, Atmos. Chem. Phys., 18, 9147-9159, 10.5194/acp-18-9147-2018, 2018.

Fu, X. and Wang, T.: Persistent Heavy Winter Nitrate Pollution Driven by Increased Photochemical Oxidants in Northern China, 54, 3881-3889, 10.1021/acs.est.9b07248, 2020.

Gard, E. E., Kleeman, M. J., Gross, D. S., Hughes, L. S., Allen, J. O., Morrical, B. D., Fergenson, D. P., Dienes, T., M, E. G., Johnson, R. J., Cass, G. R., and Prather, K. A.: Direct observation of heterogeneous chemistry in the atmosphere, Science (New York, N.Y.), 279, 1184-1187, 10.1126/science.279.5354.1184, 1998.

Geng, G., Zheng, Y., Zhang, Q., Xue, T., Zhao, H., Tong, D., Zheng, B., Li, M., Liu, F., Hong, C., He, K., and Davis, S. J.: Drivers of PM2.5 air pollution deaths in China 2002–2017, Nat. Geosci., 14, 645-650, 10.1038/s41561-021-00792-3, 2021.

Guo, H., Otjes, R., Schlag, P., Kiendler-Scharr, A., Nenes, A., and Weber, R. J.: Effectiveness of ammonia reduction on control of fine particle nitrate, Atmos. Chem. Phys., 18, 12241-12256, 10.5194/acp-18-12241-2018, 2018.

Herner, J. D., Ying, Q., Aw, J., Gao, O., Chang, D. P. Y., and Kleeman, M. J.: Dominant Mechanisms that Shape the Airborne Particle Size and Composition Distribution in Central California, Aerosol Sci. Technol., 40, 827-844, 10.1080/02786820600728668, 2006.

Jensen, J. B. and Nugent, A. D.: Condensational Growth of Drops Formed on Giant Sea-Salt Aerosol Particles, J. Atmos. Sci., 74, 679-697, https://doi.org/10.1175/JAS-D-15-0370.1, 2017.

Krueger, B. J., Grassian, V. H., Iedema, M. J., Cowin, J. P., and Laskin, A.: Probing Heterogeneous Chemistry of Individual Atmospheric Particles Using Scanning Electron Microscopy and Energy-Dispersive X-ray Analysis, Anal. Chem., 75, 5170-5179, 10.1021/ac034455t, 2003.

Li, C., Dai, Z., Liu, X., and Wu, P.: Transport Pathways and Potential Source Region Contributions of PM2.5 in Weifang: Seasonal Variations, Applied Sciences, 10, 2835, 2020.

https://doi.org/10.5194/egusphere-2026-2447
Preprint. Discussion started: 3 July 2026

Li, J., Cao, L., Gao, W., He, L., Yan, Y., He, Y., Pan, Y., Ji, D., Liu, Z., and Wang, Y.: Seasonal variations in the highly time-resolved aerosol composition, sources and chemical processes of background submicron particles in the North China Plain, Atmos. Chem. Phys., 21, 4521-4539, 10.5194/acp-21-4521-2021, 2021a.

Li, K., Ma, Y., Li, L., and Huang, B.: Chemical Composition and Mixing State of Fine Particles during Haze Periods in Yinchuan, Aerosol Air Qual. Res., 23, 230116, 10.4209/aaqr.230116, 2023.

Li, L., Huang, Z., Dong, J., Li, M., Gao, W., Nian, H., Fu, Z., Zhang, G., Bi, X., Cheng, P., and Zhou, Z.: Real time bipolar time-of-flight mass spectrometer for analyzing single aerosol particles, Int. J. Mass Spectrom., 303, 118-124, https://doi.org/10.1016/j.ijms.2011.01.017, 2011.

Li, M., Zhang, Z., Yao, Q., Wang, T., Xie, M., Li, S., Zhuang, B., and Han, Y.: Nonlinear responses of particulate nitrate to NOx emission controls in the megalopolises of China, Atmos. Chem. Phys., 21, 15135-15152, 10.5194/acp-21-15135-2021, 2021b.

Lian, X., Xu, Y., Liu, F., Peng, L., Hu, X., Tang, G., Dao, X., Guo, H., Wang, L., Huang, B., Cheng, C., Li, L., Zhang, G., Bi, X., Wang, X., Zhou, Z., and Li, M.: Characterizing lead-rich particles in Beijing's atmosphere following coal-to-gas conversion: insights from single-particle aerosol mass spectrometry, Atmos. Chem. Phys., 25, 8891-8905, 10.5194/acp-25-8891-2025, 2025.

Liu, Z., Chen, H., Li, L., Xie, G., Ouyang, H., Tang, X., Ju, R., Li, B., Zhang, R., and Chen, J.: Real-time single particle characterization of oxidized organic aerosols in the East China Sea, npj Clim. Atmos. Sci., 5, 47, 10.1038/s41612-022-00267-1, 2022.

Ren, C., Huang, X., Wang, Z., Sun, P., Chi, X., Ma, Y., Zhou, D., Huang, J., Xie, Y., Gao, J., and Ding, A.: Nonlinear response of nitrate to NO(x) reduction in China during the COVID-19 pandemic, Atmospheric environment (Oxford, England : 1994), 264, 118715, 10.1016/j.atmosenv.2021.118715, 2021a.

Ren, R., Li, Z., Yan, P., Wang, Y., Wu, H., Cribb, M., Wang, W., Jin, X., Li, Y., and Zhang, D.: Measurement report: The effect of aerosol chemical composition on light scattering due to the hygroscopic swelling effect, Atmos. Chem. Phys., 21, 9977-9994, 10.5194/acp-21-9977-2021, 2021b.

Song, S., Nenes, A., Gao, M., Zhang, Y., Liu, P., Shao, J., Ye, D., Xu, W., Lei, L., Sun, Y., Liu, B., Wang, S., and McElroy, M. B.: Thermodynamic Modeling Suggests Declines in Water Uptake and Acidity of Inorganic Aerosols in Beijing Winter Haze Events during 2014/2015–2018/2019, Environ. Sci. Technol. Lett., 6, 752-760, 10.1021/acs.estlett.9b00621, 2019.

Sun, J., Li, Y., Xu, W., Zhou, W., Du, A., Li, L., Du, X., Huang, F., Li, Z., Zhang, Z., Wang, Z., and Sun, Y.: Single-particle volatility and implications for brown carbon absorption in Beijing, China, The Science of the total environment, 854, 158874, 10.1016/j.scitotenv.2022.158874, 2023.

Tao, J., Huang, J., Bian, G., Zhang, L., Zhou, Z., Zhang, Z., Li, J., Miao, Y., Yuan, Z., Sha, Q., Xiao, L., and Wang, B.: Fine particulate pollution driven by nitrate in the moisture urban atmospheric environment in the Pearl River Delta region of south China, J Environ Manage, 326, 116704, 10.1016/j.jenvman.2022.116704, 2023.

Tian, Y., Yang, T., Li, H., Tian, P., Song, Y., Tan, Y., Sun, Y., and Wang, Z.: Vertically Resolved Formation Mechanisms of Fine Particulate Nitrate in Asian Megacities: Synergistic Lidar-Aircraft Observations and Process-Based Analysis, EGUsphere, 2025, 1-22, 10.5194/egusphere-2025-898, 2025.

Wang, Y. Q., Zhang, X. Y., and Draxler, R. R.: TrajStat: GIS-based software that uses various trajectory statistical analysis methods to identify potential sources from long-term air pollution measurement data, Environmental Modelling & Software, 24, 938-939, https://doi.org/10.1016/j.envsoft.2009.01.004, 2009.

Xie, X., Hu, J., Qin, M., Guo, S., Hu, M., Wang, H., Lou, S., Li, J., Sun, J., Li, X., Sheng, L., Zhu, J., Chen, G., Yin, J., Fu, W., Huang, C., and Zhang, Y.: Modeling particulate nitrate in China: Current findings and future directions, Environ Int, 166, 107369, 10.1016/j.envint.2022.107369, 2022.

Xie, Y., Wang, G., Wang, X., Chen, J., Chen, Y., Tang, G., Wang, L., Ge, S., Xue, G., Wang, Y., and Gao, J.: Nitrate-dominated PM2.5 and elevation of particle pH observed in urban Beijing during the winter of 2017, Atmos. Chem. Phys., 20, 5019-5033, 10.5194/acp-20-5019-2020, 2020.

Xiong, X., Wang, Z., Cheng, C., Li, M., Yun, L., Liu, S., Mao, L., and Zhou, Z.: Long-Term Observation of Mixing States and Sources of Vanadium-Containing Single Particles from 2020 to 2021 in Guangzhou, China, Toxics, 11, 339, 2023.

Xu, Q., Wang, S., Jiang, J., Bhattarai, N., Li, X., Chang, X., Qiu, X., Zheng, M., Hua, Y., and Hao, J.: Nitrate dominates the chemical composition of PM(2.5) during haze event in Beijing, China, The Science of the total environment, 689, 1293-1303, 10.1016/j.scitotenv.2019.06.294, 2019.

https://doi.org/10.5194/egusphere-2026-2447
Preprint. Discussion started: 3 July 2026

Yang, L. and Bao, F.: Economic and health impacts of PM2.5 pollution in China's urban air: Assessing the financial burden, Ecotoxicology and environmental safety, 303, 118575, 10.1016/j.ecoenv.2025.118575, 2025.
Zang, H., Zhao, Y., Huo, J., Zhao, Q., Fu, Q., Duan, Y., Shao, J., Huang, C., An, J., Xue, L., Li, Z., Li, C., and Xiao, H.: High atmospheric oxidation capacity drives wintertime nitrate pollution in the eastern Yangtze River Delta of China, Atmos. Chem. Phys., 22, 4355-4374, 10.5194/acp-22-4355-2022, 2022.
Zhang, J., Chen, C., Su, Y., Guo, W., Fu, X., Long, Y., Peng, X., Zhang, W., Huang, X., and Wang, G.: Characterization of summertime single aerosol particles in Chengdu (China): Interannual evolution and impact of COVID-19 lockdown, The Science of the total environment, 907, 167765, 10.1016/j.scitotenv.2023.167765, 2024.
Zhang, Q., He, K., and Huo, H.: Cleaning China's air, Nature, 484, 161-162, 10.1038/484161a, 2012.
Zhang, Q., Meng, X., Shi, S., Kan, L., Chen, R., and Kan, H.: Overview of particulate air pollution and human health in China: Evidence, challenges, and opportunities, Innovation (Cambridge (Mass.)), 3, 100312, 10.1016/j.xinn.2022.100312, 2022.
Zheng, B., Tong, D., Li, M., Liu, F., Hong, C., Geng, G., Li, H., Li, X., Peng, L., Qi, J., Yan, L., Zhang, Y., Zhao, H., Zheng, Y., He, K., and Zhang, Q.: Trends in China's anthropogenic emissions since 2010 as the consequence of clean air actions, Atmos. Chem. Phys., 18, 14095-14111, 10.5194/acp-18-14095-2018, 2018.
Zhou, L., Liang, Z., Go, B. R., Cuevas, R. A. I., Tang, R., Li, M., Cheng, C., and Chan, C. K.: Sulfate formation via aerosol-phase SO2 oxidation by model biomass burning photosensitizers: 3,4-dimethoxybenzaldehyde, vanillin and syringaldehyde using single-particle mixing-state analysis, Atmos. Chem. Phys., 23, 5251-5261, 10.5194/acp-23-5251-2023, 2023.
Zhou, Q., Cheng, C., Yang, S., Yuan, M., Meng, J., Gong, H., Zhong, Q., Zhang, Y., Xie, Y., Zhou, Z., and Li, M.: Enhanced mixing state of black carbon with nitrate in single particles during haze periods in Zhengzhou, China, Journal of environmental sciences (China), 111, 185-196, 10.1016/j.jes.2021.03.031, 2022.
Zhou, Y., Wang, Z., Pei, C., Li, L., Wu, M., Wu, M., Huang, B., Cheng, C., Li, M., Wang, X., and Zhou, Z.: Source-oriented characterization of single particles from in-port ship emissions in Guangzhou, China, The Science of the total environment, 724, 138179, 10.1016/j.scitotenv.2020.138179, 2020.